

Terahertz emission from α -W/CoFe epitaxial spintronic emitters

Venkatesh Mottamchetty,^{1,2} Rimantas Brucas,¹ Anna L. Ravensburg,² Renan Maciel,² Danny Thonig,^{3,2} Jürgen Henk,⁴ Rahul Gupta,⁵ Arne Roos,¹ Cheuk Wai Tai,⁶ Vassilios Kapaklis,² and Peter Svedlindh^{1,*}

¹*Department of Materials Science and Engineering,
Uppsala University, Box 35, SE-751 03 Uppsala, Sweden*

²*Department of Physics and Astronomy, Uppsala University, Box 516, 75120 Uppsala, Sweden*

³*School of Science and Technology, Örebro University, SE-70182 Örebro, Sweden*

⁴*Institut für Physik, Martin Luther University Halle-Wittenberg, 06099 Halle, Germany*

⁵*Department of Physics, University of Gothenburg, Gothenburg 412 96, Sweden*

⁶*Department of Materials and Environmental Chemistry, Stockholm University, 10691 Stockholm, Sweden*

(Dated: October 11, 2024)

We report efficient terahertz (THz) generation in epitaxial α -W/Co₆₀Fe₄₀ spintronic emitters. Two types of emitters have been investigated; epitaxial α -W(110)/Co₆₀Fe₄₀(110) and α -W(001)/Co₆₀Fe₄₀(001) deposited on single crystalline Al₂O₃(1120) and MgO(001) substrates, respectively. First principle calculations of the electronic band structure at the W(001) surface reveal Dirac-type surface states, similar to that reported previously for the W(110) surface. The generated THz radiation is about 10% larger for α -W(110)/Co₆₀Fe₄₀(110) grown on single crystalline Al₂O₃(1120), which is explained by the fact that the α -W(110)/Co₆₀Fe₄₀(110) interface for this emitter is more transparent to the spin current due to the presence of Ångström-scale interface intermixing at the W/CoFe interface. Our results also reveal that the generation of THz radiation is larger when pumping with the laser light from the substrate side, which is explained by a larger part of the laser light due to interference effects in the film stack being absorbed in the ferromagnetic Co₆₀Fe₄₀ layer in this measurement configuration.

I. INTRODUCTION

Terahertz (THz) radiation is typically defined from 0.3 to 30 THz of the electromagnetic spectrum corresponding to a wavelength range of 1 mm to 10 μ m. The terahertz frequency range lies between the microwave and near-infrared regions of the electromagnetic spectrum and has traditionally been called the terahertz gap due to the difficulties in generating THz radiation. This has limited its use despite of a large number of possible applications [1–3]. Techniques used for generation of THz radiation include photoconductive switching, optical rectification, transient photo-current in air plasma and difference frequency generation [4–13]. A more recent technique builds on the spin degree of freedom in magnetic heterostructures [14–16]. This technique has the advantage of generating broadband radiation and with intensity levels comparable to the standard zinc telluride source.

A magnetic heterostructure generating THz radiation, referred to as a spintronic THz emitter (STE), typically consists of a heavy metal (HM) with strong spin-orbit interaction and a ferromagnetic (FM) material. It is well established that a femto-second laser pulse leads to a demagnetization process of the FM layer and the generation of an ultrafast superdiffusive spin current (j_s) [17, 18]. The transfer of spin current across the FM/HM interface will via the inverse spin Hall effect (ISHE) [19] or the inverse Rashba-Edelstein effect (IREE) [20] generate a transient charge current (j_c) in the HM layer that emits

THz radiation. Critical parameters for the emission of THz radiation are the spin-to-charge conversion efficiency characterized by the spin Hall angle (θ_{SHE}) of the HM, $\theta_{SHE} = j_s/j_c$, and the transparency of the FM/HM interface characterized by the effective spin-mixing conductance ($g_{eff}^{\uparrow\downarrow}$) of the interface [21–23]. The effective spin-mixing conductance describes the transfer of spin current across the interface and accounts for spin-backflow as well as spin-memory loss at the interface, emphasizing the importance of the interface quality for STEs. For example, large interface roughness may lead to spin memory loss at the interface [24].

Tungsten may crystallize in the ground-state α -W A2 phase or in the metastable β -W A15 phase. Interestingly, the high-resistivity β -W phase ($\rho \sim 150 - 300 \mu\Omega\text{cm}$) has been reported to exhibit a giant SHE with a spin Hall angle $\theta_{SHE} \sim -0.3$ to -0.4 [25–27], while the low-resistivity α -W phase ($\rho \sim 20 \mu\Omega\text{cm}$) exhibits a more modest value of the spin Hall angle ($\theta_{SHE} \sim -0.07$). *Ab initio* electronic structure calculations have revealed that the spin Hall conductivity (σ_{SHE}) for the β -W phase is about 60% larger than that of the α -W phase [26]. It is clear that this difference in spin Hall conductivity alone cannot explain the difference in spin Hall angle. However, considering that the spin Hall angle can be expressed as $\theta_{SHE} = \rho\sigma_{SHE}$, it becomes clear that the difference is a combined effect of the spin Hall conductivity and the much larger resistivity of the β -W phase.

It has been argued from first-principle calculations that the Dirac fermions appearing in the β -W phase are important to understand its giant spin Hall effect [28], since according to a separate study, Dirac fermions have been identified to generate Berry-curvature-induced spin Hall

* peter.svedlindh@angstrom.uu.se

conductivity [29]. Interestingly, the presence of topological surface states in tungsten was first predicted by Thonig *et al.* [30] for the α -W phase. Moreover, it has been reported that these surface states predominately appear in certain crystallographic planes [28, 30, 31].

In this study, we have investigated the THz emission from epitaxial α -W/Co₆₀Fe₄₀ spintronic emitters. Two types of emitters have been investigated, deposited on single crystalline Al₂O₃ (11 $\bar{2}$ 0) and MgO (001) substrates. A strong motivation for choosing these substrates is that they provide two different interfaces for tungsten; namely α -W (110) in case of Al₂O₃ (11 $\bar{2}$ 0) [32] and α -W (001) in case of MgO (001) [33]. It has been shown that the α -W(110) interface exhibits Dirac-type surface states [30], which is believed to have a direct impact on the spin Hall angle and therefore also on the spin-to-charge conversion of the STE. It is therefore motivated to investigate if the two interfaces are different in this respect and if there are other interface related properties that may affect the emission of THz radiation.

II. METHODS

A. Growth

Magnetic heterostructures consisting of α -W/Co₆₀Fe₄₀ (henceforth referred to as W/CoFe) bilayers with different layer thicknesses ranging from 2 to 4 nm were deposited on single crystalline Al₂O₃ (11 $\bar{2}$ 0) and MgO (001) substrates (both 10×10 mm²) at floating potential, using direct current (dc) magnetron sputtering. Except for the W(t_W)/CoFe(3) series of samples (t_W is the thickness of the W-layer; numbers within parentheses refer to layer thickness in nm), which were deposited on double-sided polished Al₂O₃ (11 $\bar{2}$ 0), the films were deposited on single-sided polished substrates. Prior to deposition, the substrates were cleaned in acetone and 2-propanol using ultrasonic agitation for 120 s each. This was followed by annealing in vacuum at 873(2) K for 1 hour. The base pressure of the growth chamber was below 5×10^{-7} Pa. In order to prevent surface oxidation of the films, the samples were capped at ambient temperature (< 313(2) K) with Al₂O₃ (nominal thickness 6 nm) using radio frequency (rf) magnetron sputtering. The depositions were carried out in an Ar atmosphere at a pressure of 3×10^{-2} Pa (gas purity ≥ 99.999 %) from an elemental W (25 W, dc) target, and CoFe (13 W, dc) and Al₂O₃ (90 W, rf) compound targets. The targets were cleaned by sputtering against closed shutters for at least 60 s prior to each deposition. The target-to-substrate distance in the deposition chamber was around 0.2 m. The deposition rates (W: 0.253 Å/s, Al: 0.30 Å/s, CoFe: 0.10 Å/s, Al₂O₃: 0.03 Å/s) were calibrated prior to the growth using X-ray reflectivity. The W growth temperature was optimized with respect to W layering and crystal quality, yielding 843(2) K for single W layers. For the W/CoFe bilayers, W and CoFe were grown

at 843(2) K and 573(2) K, respectively. Finally, in order to ensure thickness uniformity, the substrate holder was rotated during the deposition.

B. Characterization

A THz time-domain spectrometer was employed to measure the THz emission from the W/CoFe heterostructures [15, 34]. This spectrometer utilized a Spectra-Physics Tsunami laser source, which generated pulses with a duration of ~ 55 fs (bandwidth ~ 12 nm, central wavelength ~ 800 nm, and maximum output energy ~ 10 nJ) at a repetition rate of 80 MHz. A low-temperature gallium arsenide photoconductive dipole antenna with ~ 4 μ m gap was used as a detector for the THz pulses. A probe beam with an average laser power of 10 mW was used for the detection and a static in-plane magnetic field of ~ 85 mT was used to saturate the magnetization of the W/CoFe films. Recorded THz signals correspond to averages of 500 detected THz spectra obtained within one minute of measurement time.

Transmission electron microscopy (TEM) and scanning TEM (STEM) were performed in a double aberration-corrected Themis Z (Thermo Fisher), which was operated at 300 kV and equipped with a low-background double-tilt holder and a Super-X EDS detector. The aberrations were corrected up to 5th order. STEM imaging and EDS acquisition and analyses were acquired using a Thermo Fisher Velox. The convergent angle of the probe and collection angle for high-angle annular dark-field (HAADF) imaging were 16 and 63-200 mrad, respectively. TEM and selected-area electron diffraction were recorded using a Gatan OneView camera.

X-ray reflectometry (XRR) and diffraction (XRD) were carried out in a Bede D1 diffractometer equipped with a Cu K_{α_1} x-ray source operated at 35 mA and 50 kV. A circular mask (diameter: 0.005 m) and an incidence and a detector slit (both 0.0005 m) were used. For monochromatizing the beam by reducing the CuK β and CuK α_2 radiation, the setup included a Göbel mirror and a 2-bounce-crystal on the incidence side. The x-rays were detected with a Bede EDRC x-ray detector. The XRR results for the STEs studied here are presented in Supplementary Information (SI), Tables ST1-ST4. The XRD results, described elsewhere [35], show that α -W grows epitaxially in the [110] growth direction on Al₂O₃ (11 $\bar{2}$ 0) and in the [001] growth direction on MgO (001). The crystalline quality for α -W grown on Al₂O₃ is better, as indicated by a much smaller mosaic spread of the crystal plane orientations. It should be noted though that α -W grown on MgO exhibits a highly preferential [001] growth orientation.

A Quantum Design magnetic property measurement system was used to assess the magnetic properties of the samples; results from room temperature magnetization versus in-plane magnetic field measurements are pre-

sented in Supplemental Material (SM), Fig. S1. An AIT CMT-SR2000N 4-point probe measurement system was used to measure the sheet resistance of α -W films with thicknesses in the range 6 – 100 nm. The low resistivity of the measured samples (cf. Fig. S2 in SM) confirms the α -phase for the epitaxial W layers.

In an attempt to determine the optical absorptance of the investigated film stacks, reflectance (R) and transmittance (T) spectra were measured using an integrated sphere, Perkin Elmer Lambda 900 double beam spectrophotometer equipped with a 15 cm spectralon-coated sphere. The scattered and regular/specular light signals entering the sphere have to be corrected in different ways for sphere wall reflectance and hence, both total and scattered spectra were recorded in both reflectance and transmittance modes [36–38]. The absorptance was then calculated as $A = 1 - R - T$. The calculated absorptance is the total absorptance of the film stack. Schematic illustrations of the sphere geometry in reflectance and transmittance modes are shown in SM, Fig. S3.

Standard Fresnel calculations were performed for film stacks with different compositions and thickness [39, 40]. The film stack configuration is illustrated in SM, Fig. S4. Such calculations are to some extent uncertain because the included films are very thin, and the optical constants are slightly uncertain. It is well known that the optical constants of very thin films may differ from the optical constants of thick films or bulk materials. Calculations are useful, however, as it is simple and straight forward to vary the composition of the film stack and to get an indication of how film thickness influences the optical properties of the samples. The optical constants for the different layers and substrates used were taken from the literature [41, 42]. The optical constants for the CoFe film was taken as the average value of the constants for Co and Fe. Possible absorption in the oxide substrates was not considered in the calculations.

The spectral function of the surface band structure was simulated by density functional relativistic multiple-scattering theory [43] as formulated in the Korringa-Kohn-Rostoker (KKR) approach [44, 45] and implemented in the code *Cahmd* [46]. Relativistic effects are fully accounted by solving the Dirac equation. The surface was modelled by a semi-infinite geometry within the layer-KKR scheme [45] which excludes finite size effects and is well suited for semi-infinite systems (e.g., surfaces and interfaces). The spectral density $n_{i\alpha}(E, \mathbf{k}_{\parallel})$, i.e., the energy- and wavevector-resolved local density of states for a site α in layer i , is computed from the site-resolved Green function $G_{i\alpha, i\alpha}(E + i\eta, \mathbf{k}_{\parallel})$,

$$n_{i\alpha}(E, \mathbf{k}_{\parallel}) = -\frac{1}{\pi} \text{ImTr} G_{i\alpha, i\alpha}(E + i\eta, \mathbf{k}_{\parallel}) . \quad (1)$$

η is a small offset from the energy axis leading to a broadening of the spectral density; typically $\eta = 0.01\text{eV}$. The spectral density can further be decomposed with respect to spin polarization, thus allowing for a detailed

characterization of the electronic states. In order to account for surface relaxations, we relaxed the surface layer by -3% , similar to the proposed surface layer relaxation in W(110) discussed in Ref. [30, 47].

III. RESULTS AND DISCUSSION

HRTEM and high-resolution HAADF-STEM images of W/CoFe layers are shown in Figure 1, while HAADF-STEM images and EDS maps are presented in SM, Fig. S5. The contrast of HAADF images, known as Z-contrast, clearly distinguishes the layers, including the Al_2O_3 capping layer. The estimated thicknesses of the W and CoFe layers are 3.2 nm and 3.4 nm on the Al_2O_3 substrate and 3.2 nm and 3.2 nm on the MgO substrate, respectively. The EDS maps confirm that the element distributions are confined in each layer. High-resolution HAADF-STEM images, shown in Fig. 1 (c) and (d), illustrate the epitaxial relationship between substrate and layers by the alignment of lattice planes. In the case of the MgO substrate, the interface between the W and CoFe layers is atomically flat, while a few atomic layers intermixing at the interface is observed for the Al_2O_3 substrate. In addition to HAADF-STEM imaging, HRTEM images were taken in order to obtain other information than atomic species and thickness. Figure 1 (a) and (b) show the HRTEM images of W/CoFe on Al_2O_3 and MgO substrate, respectively. The alignment of lattice planes in W, CoFe and the substrates are consistent with the HAADF results.

The insets in Figure 1 (a) and (b) are the fast Fourier transform (FFT) of the HRTEM images, which are similar to selected area electron diffraction patterns shown in SM, Figs. S6 and S7. In addition, the FFTs of the selected regions, highlighted in red squares, show the orientations. All FFTs confirm the epitaxial relationship. In the case of the Al_2O_3 substrate (Fig. 2 (a)), the interface between the W and CoFe layers looks smoother than indicated by HAADF-STEM. It is worth noting that the imaging mechanisms of HRTEM are phase and diffraction contrast that are sensitive to crystallographic orientation and defects but not to the atomic number as in HAADF. The asymmetric contrasts of different lattice fringes indicate a slight but detectable crystallographic misorientation from the zone axis. By contrast, the interface in the film deposited on MgO exhibits more localized bright/dark contrasts. These additional contrasts indicate the presence of local strain, where distortion of lattice fringes and edge dislocations are expected.

Figure 2(a) shows the generated THz electric field in time domain for W/CoFe STEs deposited on Al_2O_3 (11 $\bar{2}$ 0) and MgO (001) substrates when pumping from the substrate side. Note that the polarity of the THz waveform is reversed when reversing the magnetization direction while keeping the pumping side the same (cf. Fig. S8 in SM). Thus, the THz emission is clearly of magnetic origin. Figure 2(b) shows the THz electric

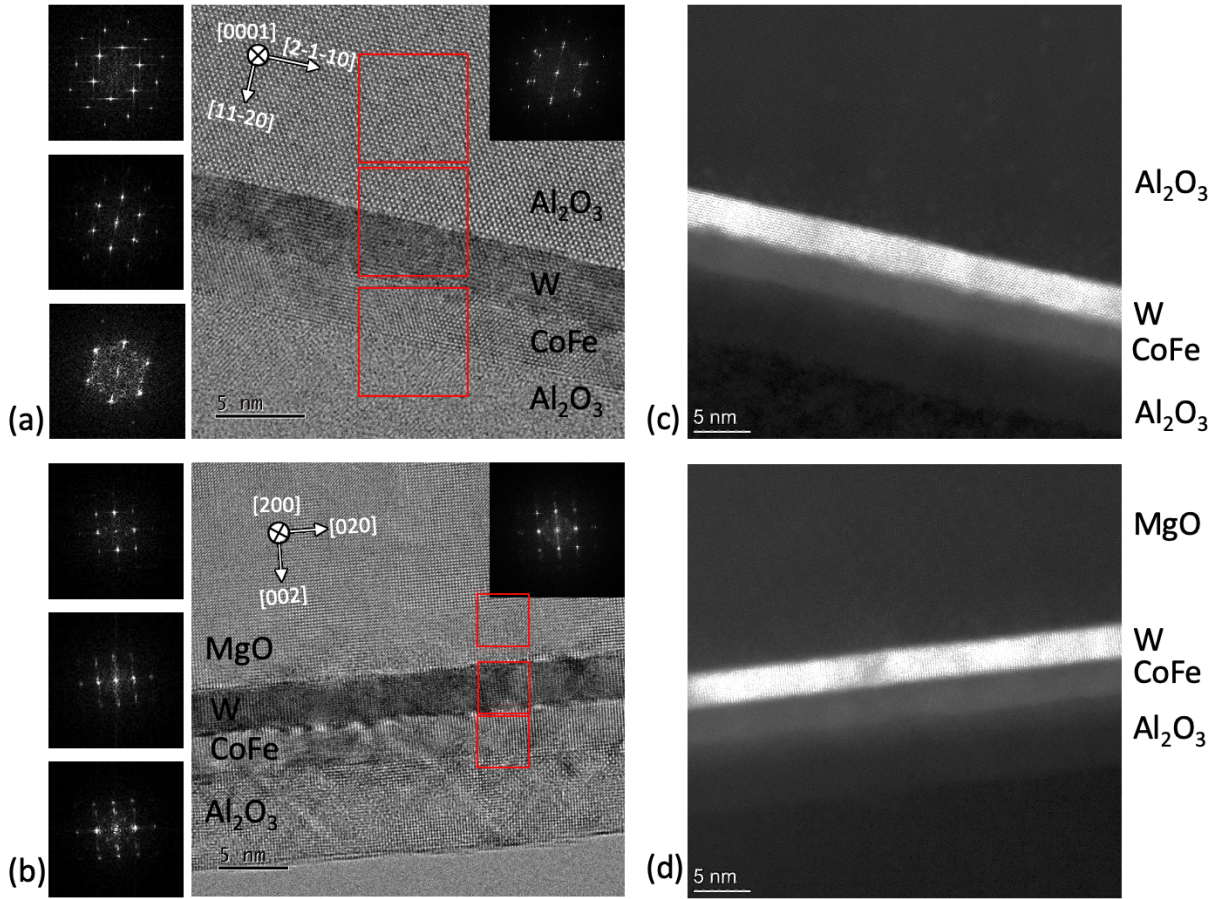


FIG. 1. HRTEM and high-resolution HAADF-STEM images of W/CoFe layers in (a,c) Al_2O_3 and (b,d) MgO substrate, respectively. Inset: overall FFT of the HRTEM image. FFT patterns of selected areas, highlighted by red squares, are also given on the left side of the images.

field peak-to-peak amplitude versus laser fluence for the same STEs. As expected, the peak-to-peak amplitude increases linearly at low laser fluence, but the increase slows down above 0.2 mJ/cm^2 laser fluence and the amplitude reaches a maximum at about 0.6 mJ/cm^2 laser fluence followed by a weak decrease of the amplitude on further increase of the laser fluence. Similar behaviour has previously been observed and can be attributed to the spin accumulation and laser-induced heating effects [48–50]. The spin accumulation effect implies that there is an upper limit for the density of spin-polarized electrons in the HM, while the heating effect induces a large enough increase of the spin temperature to weaken the magnetization of the ferromagnetic layer [51]. The variation of the THz electric field peak-to-peak amplitude with thickness of the W and CoFe layers is reported in SM, Fig. S9. The largest amplitude is obtained for a W thickness of 2.5nm and a CoFe thickness of 3nm.

Figures 2(c,d) show, respectively the THz electric field peak-to-peak amplitude for $\text{MgO}/\text{W}(3)/\text{CoFe}(2.5)/\text{Al}_2\text{O}_3(6)$ and $\text{sapphire}/\text{W}(3)/\text{CoFe}(2.5)/\text{Al}_2\text{O}_3(6)$ versus laser fluence when pumping from the substrate and film sides. For

both STEs, the generated THz electric field is significantly larger when pumping from the substrate side. The only plausible explanation for this is that more laser fluence is absorbed when pumping from the substrate side and that therefore a larger spin current is generated. This will be further discussed below.

Figure 2 also indicates that the emitted THz electric field is about 10% larger for the STE grown on the Al_2O_3 (11 $\bar{2}$ 0) substrate. It is tempting to attribute this difference to the Dirac-type surface states shown to exist in α -W(110) [30]. To investigate this in more detail, we have performed first principle calculations for α -W to probe the electronic band structure in the bulk as well as at the W(001) surface. The electronic structure of the W(110) is already published by the authors in Refs. [30, 47]. Similar to the therein reported Dirac-type surface states (DSS), we identified two Dirac-type states also in the (001)-crystallographic plane (see Fig. 3), one at the $\bar{\Gamma}$ -point and one at $E_F - 0.6 \text{ eV}$. Opposite to (110), the DSS in the (001) plane is linear only very close to the $\bar{\Gamma}$ -point. The orbital decomposition of the top layer's spectral function is z^2 , same as in W(110).

The spin texture exhibits characteristics of the Rashba

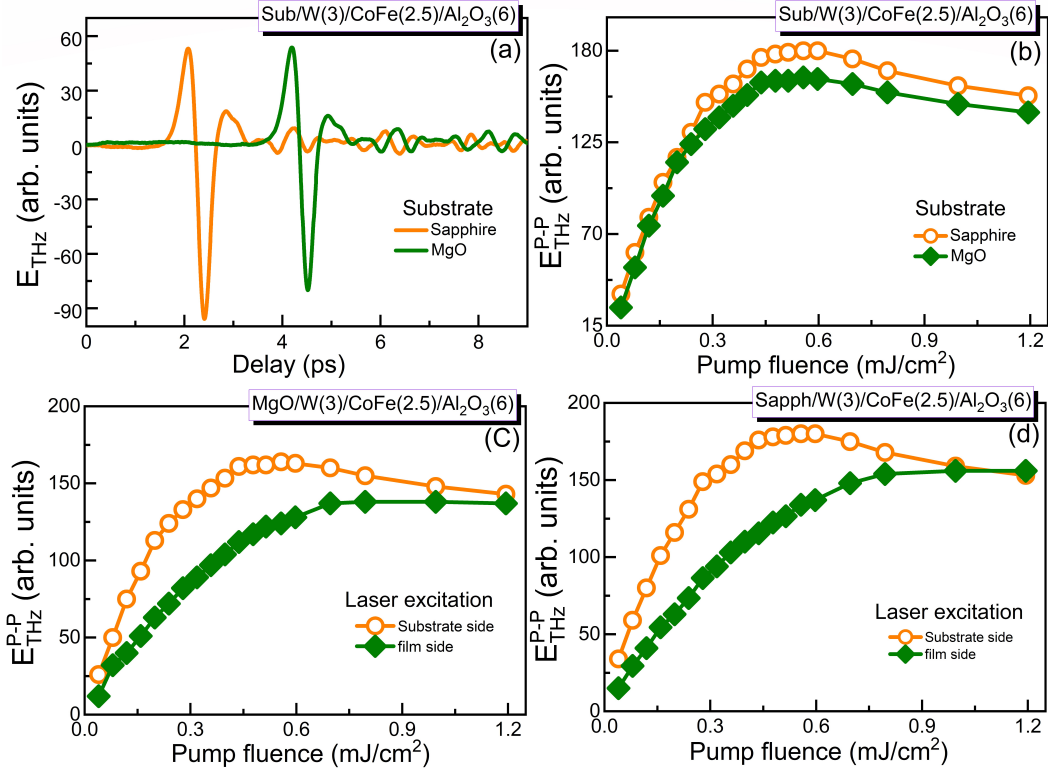


FIG. 2. (a) THz electric field waveform in time-domain for substrate/W(3)/CoFe(2.5)/Al₂O₃(6) when pumping from substrate side using 0.3 mJ/cm² laser fluence. (b) THz electric field peak-to-peak amplitude for substrate/W(3)/CoFe(2.5)/Al₂O₃(6) versus laser fluence. (c) THz electric field peak-to-peak amplitude for MgO/W(3)/CoFe(2.5)/Al₂O₃(6) versus laser fluence when pumping from the substrate and film sides. (d) THz electric field peak-to-peak amplitude for sapphire/W(3)/CoFe(2.5)/Al₂O₃(6) versus laser fluence when pumping from the substrate and film sides.

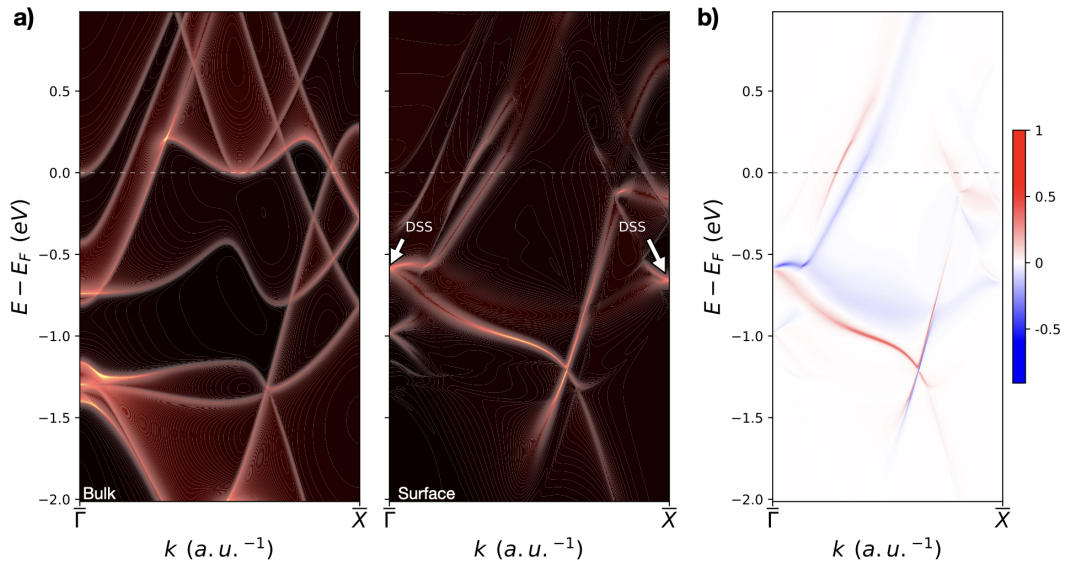


FIG. 3. Electronic band structure with marked topological surface states (DSS) of α -W (001) crystallographic planes. a) Left and right panel shows the bulk and surface band structure, respectively. b) Spin polarization (red - spin-up; blue - spin-down) of the surface states.

type, governed by both point group symmetry and time-reversal symmetry. Specifically, the spin lies in-plane and is perpendicular to the wave vector \vec{k} ; this component is often referred to as the 'Rashba component'. Time-reversal symmetry ensures that when \vec{k} is reversed to $-\vec{k}$, the spin also flips direction. Near the Dirac point, the spin polarization reaches 30% (in absolute terms), which is below that of the topological insulator Bi_2Te_3 (about 60% [52]).

The Chern number, which is determined by the number of topological surface states, is the same for both the $\text{W}(001)$ and $\text{W}(110)$ surfaces. As a result, the Berry curvature derived from the spectral function [30] is likely to be similar for both orientations. However, since the spin Hall effect (SHE) is proportional to the integrated Berry curvature, a definitive conclusion about which surface exhibits a stronger SHE would require more extensive simulations. In contrast, the conductivity of the $\text{W}(001)$ and $\text{W}(110)$ surfaces is proportional to the number of states at the Fermi energy. Because of the band touching between $\bar{\Gamma}$ and \bar{X} in $\text{W}(001)$, the conductivity in $\text{W}(001)$ is likely higher than in $\text{W}(110)$ (see spectral function of $\text{W}(110)$ in Fig. 1 of Ref. [47]).

Although an explanation based on a difference in surface electronic structure can not be ruled out, another possible explanation for the difference in THz electric field amplitude is connected to the transparency of the α - W/CoFe interface characterized by the effective spin-mixing conductance. The influence of interface intermixing on the spin-mixing conductance has been quantitatively studied for Pt/Py ($\text{Py} = \text{Permalloy}$) bilayers using first-principles calculations [53]. The interface intermixing was modelled as a scattering region consisting of composite $\text{Pt}_{1-x}\text{Py}_x$ and $\text{Pt}_x\text{Py}_{1-x}$ layers for the first Pt and Py atomic layers at the interface. Comparing with the spin-mixing conductance for an ideally clean and atomically flat interface, corresponding to $x = 0$, it was found that the spin-mixing conductance is enhanced in the presence of interface intermixing. Moreover, experimental support for this has been obtained for Co/Pt bilayers [54]. An ultrathin layer of the composite $\text{Co}_x\text{Pt}_{1-x}$ was in this work introduced between the Co and Pt layers to study the effect of interface intermixing, clearly revealing that interface intermixing enhances THz emission. Based on the information obtained from the high-resolution HAADF-STEM images, we conclude that the enhanced THz electric field amplitude for the STE grown on the Al_2O_3 ($11\bar{2}0$) substrate is likely a result of an Ångström-scale scattering region at the interface consisting of a few atomic composite layers as described in the first-principles calculations [53]. Considering the high crystalline quality of the bilayers studied here, we are not considering the effect of strongly disordered interfaces on the spin-mixing conductance and THz emission.

It is interesting to compare the α - $\text{W}/\text{Co}_{60}\text{Fe}_{40}$ STE investigated here with a standard bilayer STE like Fe/Pt [50]. We therefore deposited a $\text{MgO}/\text{Fe}(3)/\text{Pt}(3)$ STE for comparison with our α - W based STEs. Figures 4 (a)

and (b) show the THz electric field waveform in time domain and the peak-to-peak amplitude versus laser power for $\text{MgO}/\text{W}(3)/\text{CoFe}(3)$ and $\text{MgO}/\text{Fe}(3)/\text{Pt}(3)$, respectively. The emitted THz signals are comparable for these two STEs, even though it should be noted that the $\text{MgO}/\text{Fe}/\text{Pt}$ STE exhibits larger THz amplitude decreasing the thickness of the Pt layer (cf. Fig. S10 in SM).

There is a considerable difference in optical properties between the two measurement orientations, as light beams reflected from the two surfaces of the substrate are non-coherent and are not subject to interference effects. The aluminium-oxide cap on the film side, on the other hand, is very thin and thus interference occurs between multiply reflected beams. The surface texture of the back surface of the substrate also causes light to be scattered in different ways in the front and back configurations. These two effects result in the fact that the transmittance and reflectance spectra are different for the two measurement orientations. The difference in absorptance caused by interference is illustrated in Fig. 5(a), where the reflectance, transmittance and absorptance spectra for the $\text{W}(3)/\text{CoFe}(3)$ emitter are shown. This sample was prepared on a double-sided polished Al_2O_3 ($11\bar{2}0$) substrate, implying that there is no surface texture on the back surface of the substrate. It can be seen that for this sample the reflectance is quite different between the light being incident from the substrate and film sides while the transmittance is the same. In both orientations the diffuse signals are close to zero. This means that the absorptance is higher for light incident from the substrate side, which in turn implies that one can expect a stronger spin current j_s to be generated for this orientation.

For the other STEs the surface texture on the back surface of the substrate causes diffuse (scattered) signals, which complicates the situation. The transmittance is in these cases not the same from the two sides and both reflectance and transmittance differ. This can be seen in Fig. S11 in SM. However, accounting for the diffuse scattering it can be seen that the absorptance for all STEs is higher for light incident from the substrate side.

A problem with the results from calculations is that these do not take light scattering into account, but the results indicate that the trends with varied input parameters are consistent with our experimental results. The sample with a smooth back surface can be used to compare experimental and calculated results with no scattering involved. This is shown in Fig. 5(b). It can be seen that the trends with the difference in reflectance and absorptance when light is incident on the film and substrate sides of the sample are consistent. Considering the extremely thin layers these Fresnel calculations are very encouraging.

The property of interest in this investigation is thus the absorptance within the film stack. Neither the experimental results, nor the calculated results, provide information about exactly where in the film stack absorption occurs. It is obvious, however, that the absorption

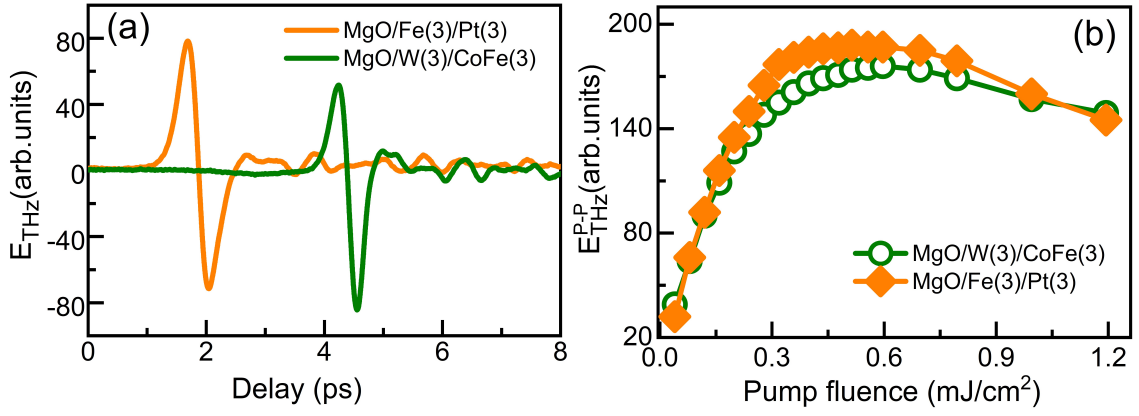


FIG. 4. (a) THz electric field waveform in time-domain for MgO/W(3)/CoFe(3) and MgO/Fe(3)/Pt(3) when pumping from the substrate side using $0.24 \text{ mJ}/\text{cm}^2$ laser fluence. (b) THz electric field peak-to-peak amplitude for MgO/W(3)/CoFe(3) and MgO/Fe(3)/Pt(3) when pumping from the substrate side versus laser fluence.

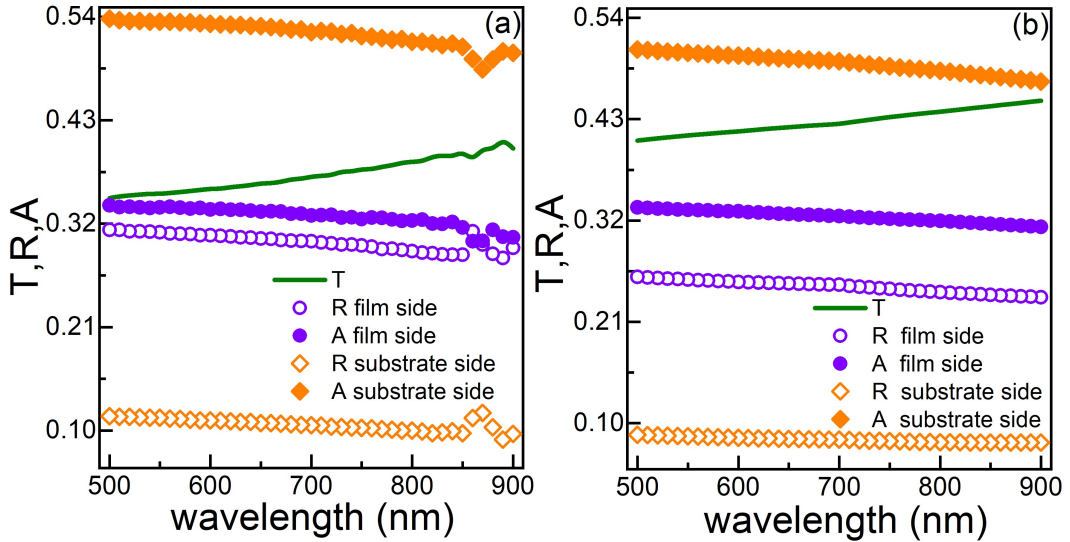


FIG. 5. Reflectance, transmittance and absorptance spectra for a smooth, non-scattering sample measured with the film and substrate sides facing the beam. It should be noted that there is no difference in transmittance between the two measurement configurations in this case. (a) Experimental results for sapphire/W(3)/CoFe(3) and (b) calculated results for sapphire/W(3)/CoFe(3).

mechanism is within the two metallic layers. Owing to the similarity of the optical constants of W, Co and Fe, the absorption is likely to be similar in the two metallic layers (W and CoFe). Both the calculated results and the experimental results indicate that the absorptance is higher when light is incident from the substrate side. The absorptance also increases with film thickness of the CoFe layer, which is also as expected. These results are shown in Fig. S12 in SM for the measured and calculated absorptance. The trend is the same for all results, but there is a difference as the experimental results take light scattering into account while the calculated spectra assume ideally flat interfaces.

An unexpected result was revealed when comparing the THz emission between STEs grown on double-sided

and single-sided polished substrates. THz electric field in time domain for sapphire/W(3)/CoFe(3)/ $\text{Al}_2\text{O}_3(6)$ and MgO/W(3)/CoFe(3)/ $\text{Al}_2\text{O}_3(6)$ when pumping from substrate and film sides are shown in Fig. S13 in SM. The former STE was grown on double-sided polished substrate, while the latter was grown on single-sided polished substrate. The THz electric field amplitude is about 30% larger for the film grown on the double-sided polished substrate when pumping from the substrate side. A possible explanation for this result is that the substrates used in this study have some absorption. When pumping from the substrate side, considering light scattering at the substrate back surface, the light will travel a longer path inside the substrate thereby yielding increased absorption in the substrate. Increased absorption in the substrate

in turn implies less light reaching the magnetic layer and therefore a reduced spin current j_s and emission of THz radiation.

IV. CONCLUSION

To summarize, we provide direct evidence of THz emission in epitaxial α -W/Co₆₀Fe₄₀ spintronic emitters. Two types of emitters have been investigated; epitaxial α -W(110)/Co₆₀Fe₄₀(110) and α -W(001)/Co₆₀Fe₄₀(001) deposited on single crystalline Al₂O₃(11 $\bar{2}$ 0) and MgO(001) substrates, respectively. The generated THz radiation is about 10% larger for the α -W(110)/Co₆₀Fe₄₀(110) emitter, which might be linked to a difference in Dirac surface states appearing in α -W(110) and α -W(001). Even if an explanation based on a difference in surface electronic structure can not be ruled out, a more likely explanation is that the α -W(110)/Co₆₀Fe₄₀(110) interface is more transparent to the spin current due to the presence of Ångström-scale interface intermixing at the W/CoFe interface. Results from first-principles calculations show that the spin-mixing conductance is enhanced in the presence of interface intermixing [53]. Our results also reveal that the generation of THz radiation is larger when pumping with the laser light from the substrate side. Measurements of reflectance and transmittance spectra as well as Fresnel calculations for the studied film stacks show that this can be explained by a larger part of the laser light being absorbed in the ferromagnetic Co₆₀Fe₄₀ layer in this measurement configuration due to interference effects.

A comparison with the reference Fe/Pt STE, which is known to provide one of the highest THz signals [16], shows that the emitted W/CoFe THz electric field amplitude is of similar magnitude. It is also worth noting that light scattering at the substrate back surface may suppress the amplitude of the emitted THz electric field amplitude by increased absorption of the laser light in the substrate.

V. ACKNOWLEDGMENTS

This work is supported by the Swedish Research Council (grant numbers 2023-04239, 2021-04658, 2019-03666, and 2019-03581), Olle Engkvists Stiftelse (grant number 182-0365) and the Deutsche Forschungsgemeinschaft (DFG, German Research Foundation) – Project-ID 328545488 – TRR 227, project B04. This work was performed, in part, at the Electron Microscopy Centre, supported by the Department of Materials and Environmental Chemistry and Faculty of Science at Stockholm University, Sweden.

VI. AUTHOR CONTRIBUTIONS

VM, RB, RG, VK, and PS contributed to the conception and design of the study. Material preparation, data collection and analysis were performed by VM, RB, ALR, AR, CWT and PS. Theoretical calculations were performed by RM, DT and JH. PS supervised the project. The first draft of the manuscript was written by PS with contributions from VM, DT, AR and CWT and all authors commented on previous versions of the manuscript. All authors read and approved the final manuscript.

-
- [1] G. Valušis, A. LISAUSKAS, H. Yuan, W. Knap, and H. G. Roskos, *Sensors* **21** (2021).
- [2] J. Federici and L. Moeller, *J. Appl. Phys.* **107**, 6 (2010).
- [3] A. Leitenstorfer, A. S. Moskalenko, T. Kampfrath, J. Kono, E. Castro-Camus, K. Peng, N. Qureshi, D. Turchinovich, K. Tanaka, A. G. Markelz, M. Havenith, C. Hough, H. J. Joyce, W. J. Padilla, B. Zhou, K.-Y. Kim, X.-C. Zhang, P. U. Jepsen, S. Dhillon, M. Vitiello, E. Linfield, A. G. Davies, M. C. Hoffmann, R. Lewis, M. Tonouchi, P. Klarskov, T. S. Seifert, Y. A. Gerasimenko, D. Mihailovic, R. Huber, J. L. Boland, O. Mitrofanov, P. Dean, B. N. Ellison, P. G. Huggard, S. P. Rea, C. Walker, D. T. Leisawitz, J. R. Gao, C. Li, Q. Chen, G. Valušis, V. P. Wallace, E. Pickwell-MacPherson, X. Shang, J. Hesler, N. Ridler, C. C. Renaud, I. Kallfass, T. Nagatsuma, J. A. Zeitler, D. Arnone, M. B. Johnston, and J. Cunningham, *Journal of Physics D: Applied Physics* **56**, 223001 (2023).
- [4] P. R. Smith, D. H. Auston, and M. C. Nuss, *IEEE Journal of Quantum Electronics* **24**, 255 (1988).
- [5] M. Venkatesh, K. Rao, T. Abhilash, S. Tewari, and A. Chaudhary, *Optical Materials* **36**, 596 (2014).
- [6] S. Lepeshov, A. Gorodetsky, A. Krasnok, E. Rafailov, and P. Belov, *Laser & Photonics Reviews* **11**, 1600199 (2017).
- [7] Z. Yang, L. Mutter, M. Stillhart, B. Ruiz, S. Aravazhi, M. Jazbinsek, A. Schneider, V. Gramlich, and P. Günter, *Advanced Functional Materials* **17**, 2018 (2007).
- [8] S.-J. Kim, B. J. Kang, U. Puc, W. T. Kim, M. Jazbinsek, F. Rotermund, and O.-P. Kwon, *Advanced Optical Materials* **9**, 2101019 (2021).
- [9] S. VEDIYAPPAN, A. K. Chaudhary, V. Mottamchetty, R. Arumugam, V. Gandhiraj, M. Senthil Pandian, and R. Perumalsamy, *Crystal Growth & Design* **19**, 6873 (2019).
- [10] K.-Y. Kim, J. H. Glowina, A. J. Taylor, and G. Rodriguez, *Optics express* **15**, 4577 (2007).
- [11] D. Yan, Y. Wang, D. Xu, P. Liu, C. Yan, J. Shi, H. Liu, Y. He, L. Tang, J. Feng, *et al.*, *Photonics Research* **5**, 82 (2017).
- [12] C. Lu, C. Zhang, L. Zhang, X. Wang, and S. Zhang, *Physical Review A* **96**, 053402 (2017).
- [13] J. A. Fülöp, S. Tzortzakakis, and T. Kampfrath, *Advanced Optical Materials* **8**, 1900681 (2020).

- [14] T. Seifert, S. Jaiswal, U. Martens, J. Hannegan, L. Braun, P. Maldonado, F. Freimuth, A. Kronenberg, J. Henrizi, I. Radu, *et al.*, **Nat. Photonics** **10**, 483 (2016).
- [15] R. Gupta, S. Husain, A. Kumar, R. Brucas, A. Rydberg, and P. Svedlindh, **Adv. Opt. Mater.** **9**, 2001987 (2021).
- [16] E. T. Papaioannou and R. Beigang, **Nanophotonics** **10**, 1243 (2021).
- [17] M. Battiato, K. Carva, and P. M. Oppeneer, **Phys. Rev. Lett.** **105**, 027203 (2010).
- [18] R. Gupta, F. Cosco, R. S. Malik, X. Chen, S. Saha, A. Ghosh, T. Pohlmann, J. R. L. Mardegan, S. Francoual, R. Stefanuik, J. Söderström, B. Sanyal, O. Karis, P. Svedlindh, P. M. Oppeneer, and R. Knut, **Phys. Rev. B** **108**, 064427 (2023).
- [19] J. Sinova, S. O. Valenzuela, J. Wunderlich, C. H. Back, and T. Jungwirth, **Rev. Mod. Phys.** **87**, 1213 (2015).
- [20] J. C. R. Sánchez, L. Vila, G. Desfonds, S. Gambarelli, J. P. Attané, J. M. De Teresa, C. Magén, and A. Fert, **Nature Communications** **4**, 2944 (2013).
- [21] Y. Tserkovnyak, A. Brataas, and G. E. W. Bauer, **Phys. Rev. B** **66**, 224403 (2002).
- [22] T. H. Dang, J. Hawecker, E. Rongione, G. Baez Flores, D. Q. To, J. C. Rojas-Sanchez, H. Nong, J. Mangeney, J. Tignon, F. Godel, S. Collin, P. Seneor, M. Bibes, A. Fert, M. Anane, J.-M. George, L. Vila, M. Cosset-Cheneau, D. Dolfi, R. Lebrun, P. Bortolotti, K. Belashchenko, S. Dhillon, and H. Jaffrès, **Applied Physics Reviews** **7**, 041409 (2020).
- [23] R. Gupta, N. Behera, V. A. Venugopal, S. Basu, A. K. Puri, P. Ström, M. A. Gubbins, L. Bergqvist, R. Brucas, P. Svedlindh, and A. Kumar, **Phys. Rev. B** **101**, 024401 (2020).
- [24] K. Gupta, R. J. H. Wesselink, R. Liu, Z. Yuan, and P. J. Kelly, **Phys. Rev. Lett.** **124**, 087702 (2020).
- [25] C.-F. Pai, L. Liu, Y. Li, H. W. Tseng, D. C. Ralph, and R. A. Buhrman, **Applied Physics Letters** **101**, 122404 (2012).
- [26] X. Sui, C. Wang, J. Kim, J. Wang, S. H. Rhim, W. Duan, and N. Kioussis, **Phys. Rev. B** **96**, 241105 (2017).
- [27] Q. Hao and G. Xiao, **Phys. Rev. Appl.** **3**, 034009 (2015).
- [28] J. Li, S. Ullah, R. Li, M. Liu, H. Cao, D. Li, Y. Li, and X.-Q. Chen, **Phys. Rev. B** **99**, 165110 (2019).
- [29] L. Ye, M. Kang, J. Liu, F. von Cube, C. R. Wicker, T. Suzuki, C. Jozwiak, A. Bostwick, E. Rotenberg, D. C. Bell, L. Fu, R. Comin, and J. G. Checkelsky, **Nature** **555**, 638 (2018).
- [30] D. Thonig, T. c. v. Rauch, H. Mirhosseini, J. Henk, I. Mertig, H. Wortelen, B. Engelkamp, A. B. Schmidt, and M. Donath, **Phys. Rev. B** **94**, 155132 (2016).
- [31] J. Chakhalian, X. Liu, and G. A. Fiete, **APL Materials** **8**, 050904 (2020).
- [32] D. Choi, C. S. Kim, D. Naveh, S. Chung, A. P. Warren, N. T. Nuhfer, M. F. Toney, K. R. Coffey, and K. Barmak, **Phys. Rev. B** **86**, 045432 (2012).
- [33] P. Zheng, B. D. Ozsdolay, and D. Gall, **Journal of Vacuum Science and Technology A** **33**, 061505 (2015).
- [34] R. Gupta, E. Bagherikorani, V. Mottamchetty, M. Pavelka, K. Jatkar, D. Dancila, K. Mohammadpour-Aghdam, A. Rydberg, R. Brucas, H. A. Dürr, *et al.*, **arXiv preprint arXiv:2110.01547** (2021).
- [35] A. L. Ravensburg, R. Brucas, D. Music, L. Spode, G. K. Pálsson, P. Svedlindh, and V. Kapaklis, **Applied Physics A** **130**, 74 (2024).
- [36] J. Fendley, **Solar Energy** **35**, 281 (1985).
- [37] F. J. J. Clarke and J. A. Compton, **Color Research & Application** **11**, 253 (1986).
- [38] A. Roos, C. G. Ribbing, and M. Bergkvist, **Appl. Opt.** **27**, 3828 (1988).
- [39] M. Born and E. Wolf, *Principles of optics ; electromagnetic theory of propagation, interference, and diffraction of light* (Pergamon Press, 1975).
- [40] H. A. H. A. Macleod, *Thin-film optical filters* (Adam Hilger Ltd, 1969).
- [41] E. D. Palik, *Handbook of optical constants of solids*, Vol. II (Academic Press, Boston, Mass. ; London, 1991).
- [42] J. Weaver, C. Krafska, D. Lynch, and E. Koch, *Physics Data – Optical properties of metals* (Fachinformationszentrum Energie Physik Mathematik GMBH, Karlsruhe, 1981).
- [43] P. Weinberger, *Electron Scattering Theory of Ordered and Disordered Matter* (Clarendon Press, Oxford, 1990).
- [44] J. Zabloudil, R. Hammerling, L. Szunyogh, and P. Weinberger, eds., *Electron Scattering in Solid Matter* (Springer, Berlin, 2005).
- [45] J. Henk, in *Handbook of Thin Film Materials*, Vol. 2, edited by H. S. Nalwa (Academic Press, San Diego, 2002) p. 479.
- [46] Computer code CAHMD, classical atomistic hybrid multi-degree dynamics, using the module OMNI — Fully relativistic electron spectroscopy calculations. This module was developed by J. Henk, H. Mirhosseini, P. Bose, D. Thonig, K. Saha, N. Fomynikh, T. Scheunemann, S. V. Halilov, E. Tamura, and R. Feder (2024) (unpublished, available from <https://cahmd.gitlab.io/cahmdweb/>).
- [47] H. Mirhosseini, F. Giebels, H. Gollisch, J. Henk, and R. Feder, **New Journal of Physics** **15**, 095017 (2013).
- [48] T. Kampfrath, M. Battiato, P. Maldonado, G. Eilers, J. Nötzold, S. Mährlein, V. Zbarsky, F. Freimuth, Y. Mokrousov, S. Blügel, M. Wolf, I. Radu, P. M. Oppeneer, and M. Münzenberg, **Nature Nanotechnology** **8**, 256 (2013).
- [49] T. J. Huisman, R. V. Mikhaylovskiy, J. D. Costa, F. Freimuth, E. Paz, J. Ventura, P. P. Freitas, S. Blügel, Y. Mokrousov, T. Rasing, and A. V. Kimel, **Nature Nanotechnology** **11**, 455 (2016).
- [50] D. Yang, J. Liang, C. Zhou, L. Sun, R. Zheng, S. Luo, Y. Wu, and J. Qi, **Advanced Optical Materials** **4**, 1944 (2016).
- [51] P.-W. Ma, S. L. Dudarev, and C. H. Woo, **Phys. Rev. B** **85**, 184301 (2012).
- [52] J. Henk, A. Ernst, S. V. Eremeev, E. V. Chulkov, I. V. Maznichenko, and I. Mertig, **Physical Review Letters** **109**, 036803 (2012).
- [53] Q. Zhang, S.-i. Hikino, and S. Yunoki, **Applied Physics Letters** **99**, 172105 (2011).
- [54] G. Li, R. Medapalli, R. V. Mikhaylovskiy, F. E. Spada, T. Rasing, E. E. Fullerton, and A. V. Kimel, **Phys. Rev. Mater.** **3**, 084415 (2019).

Terahertz emission from α -W/CoFe epitaxial spintronic emitters

Venkatesh Mottamchetty,^{1,2} Rimantas Brucas,¹ Anna L. Ravensburg,²
Renan Maciel,² Danny Thonig,^{3,2} Jürgen Henk,⁴ Rahul Gupta,⁵ Arne
Roos,¹ Cheuk Wai Tai,⁶ Vassilios Kapaklis,² and Peter Svedlindh^{1,*}

¹*Department of Materials Science and Engineering,
Uppsala University, Box 35, SE-751 03 Uppsala, Sweden*

²*Department of Physics and Astronomy,
Uppsala University, Box 516, 75120 Uppsala, Sweden*

³*School of Science and Technology,
Örebro University, SE-70182 Örebro, Sweden*

⁴*Institut für Physik, Martin Luther University
Halle-Wittenberg, 06099 Halle, Germany*

⁵*Department of Physics, University of Gothenburg, Gothenburg 412 96, Sweden*

⁶*Department of Materials and Environmental Chemistry,
Stockholm University, 10691 Stockholm, Sweden*

(Dated: October 11, 2024)

* peter.svedlindh@angstrom.uu.se

I. MAGNETIZATION AND RESISTIVITY RESULTS

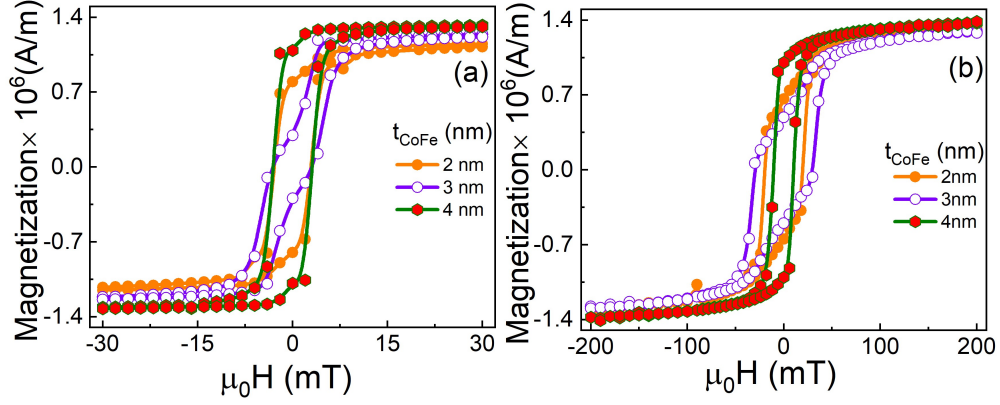


FIG. S1. Thickness dependent magnetization of (a) MgO/W(3)/CoFe(t_{CoFe})/Al₂O₃(6) and (b) Sapphire/W(3)/CoFe(t_{CoFe})/Al₂O₃(6). The saturation magnetization values are 1.40×10^6 A/m, 1.34×10^6 A/m and 1.24×10^6 A/m for $t_{CoFe} = 4, 3$ and 2 nm, respectively for the MgO substrate; the saturation magnetization values are 1.43×10^6 A/m, 1.38×10^6 A/m and 1.38×10^6 A/m for $t_{CoFe} = 4, 3$ and 2 nm, respectively for the sapphire substrate. The saturation magnetization values were calculated using the nominal thickness values.

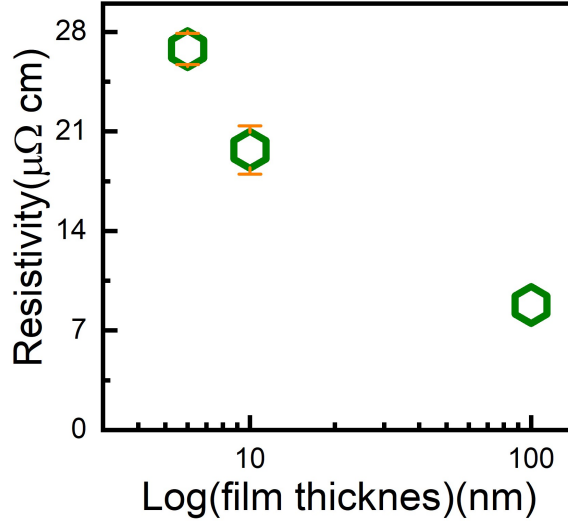


FIG. S2. Thickness dependent electrical resistivity of α -W. The increase at small thickness is due to the increased contribution from surface and interface electron scattering.

II. REFLECTANCE AND TRANSMITTANCE EXPERIMENTS

Schematic illustrations of the sphere geometry in reflectance and transmittance modes are shown in Fig. S3.

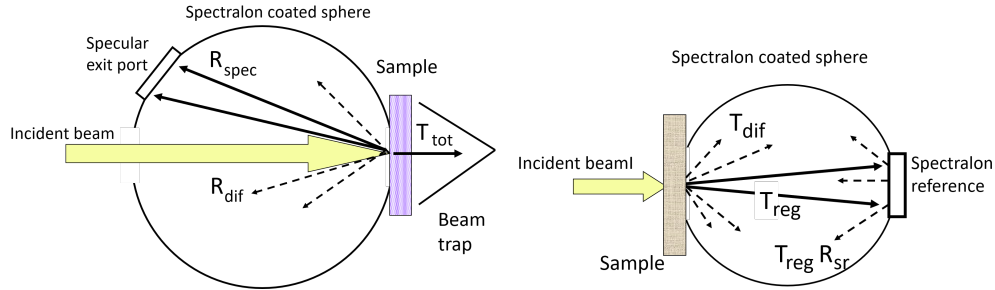


FIG. S3. Left: Schematic illustration of the integrating sphere in reflectance mode. Right: Schematic illustration of the integrating sphere in transmittance mode.

The film stack configuration is illustrated in Fig. S4 with the measured reflected and transmitted beams shown. Subscript “film” is used when incident light hits the sample from the film side and subscript “substrate” is used when incident light hits the sample from the substrate side. There is a considerable difference in the two cases, as light beams reflected from the two surfaces of the substrate are non-coherent and are not subject to interference effects. The aluminium-oxide cap on the film side, on the other hand, is very thin and thus interference occurs between multiply reflected beams. The surface texture of the back surface of the substrate also causes light to be scattered in different ways in the front and back configurations. These two effects result in the fact that the transmittance and reflectance spectra are different for the two measurement orientations.

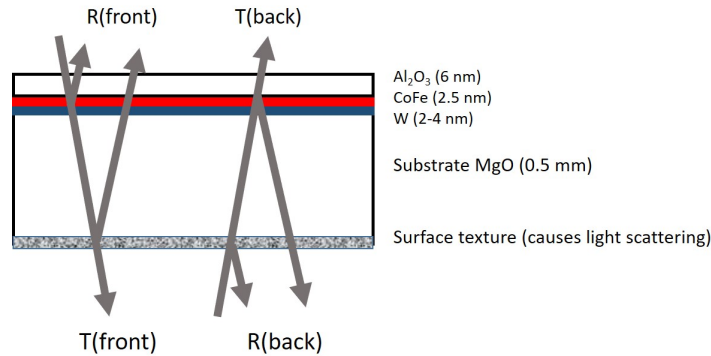


FIG. S4. Schematic illustration of the film stacks used for the experiments.

III. HAADF-STEM, EDS MAPS AND ELECTRON DIFFRACTION PATTERNS

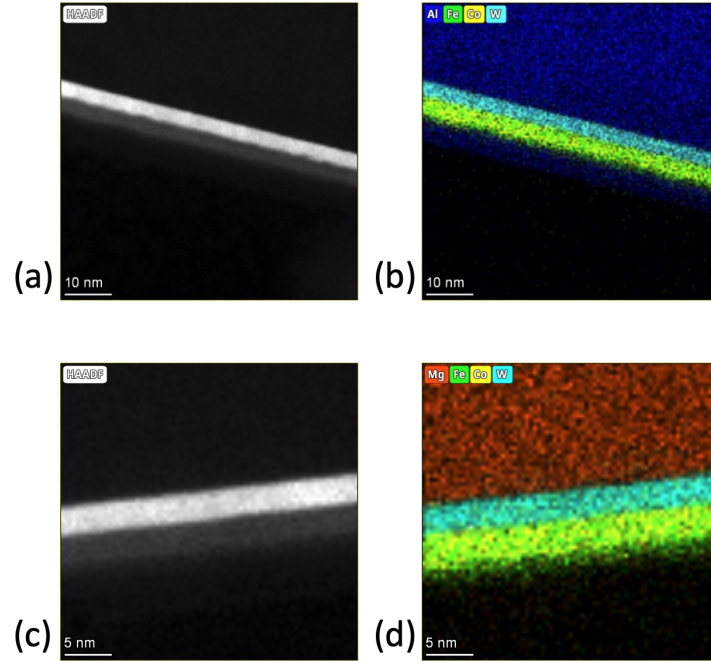


FIG. S5. (a) and (c) HAADF-STEM images of W/CoFe layers on Al₂O₃ and MgO substrate, respectively. (b) and (d) Overlay of the elements for each sample. Oxygen was omitted in order to present the elements clearly.

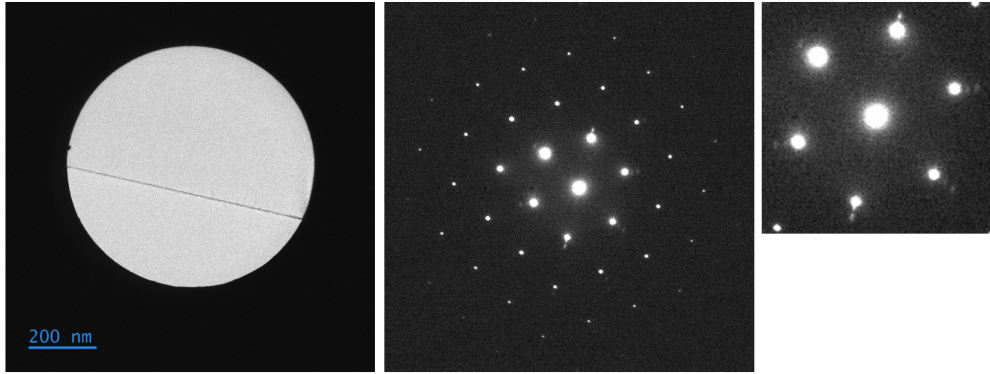


FIG. S6. Left: TEM image of W/CoFe layers on Al_2O_3 taken at lower magnification. Middle: Electron diffraction pattern of the selected area. Right: Enlarged center region of the electron diffraction pattern.

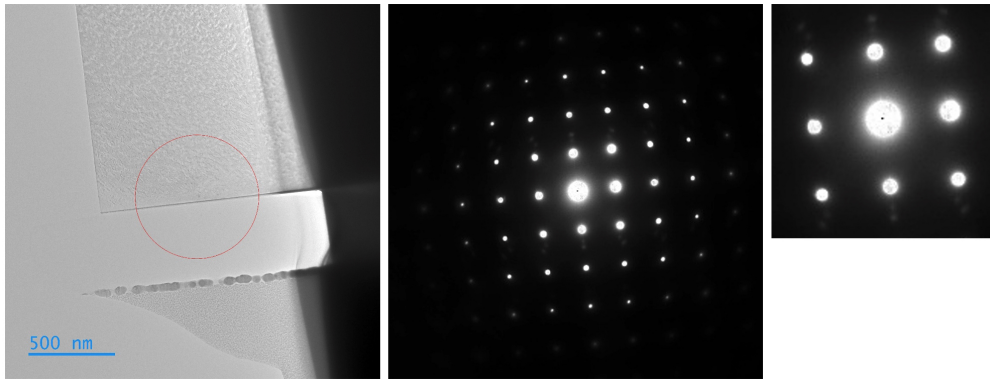


FIG. S7. Left: TEM image of W/CoFe layers on MgO taken at lower magnification. The selected area is indicated by a circle. Middle: Electron diffraction pattern of the selected area. Right: Enlarged center region of the electron diffraction pattern.

IV. RESULTS FROM THZ MEASUREMENTS

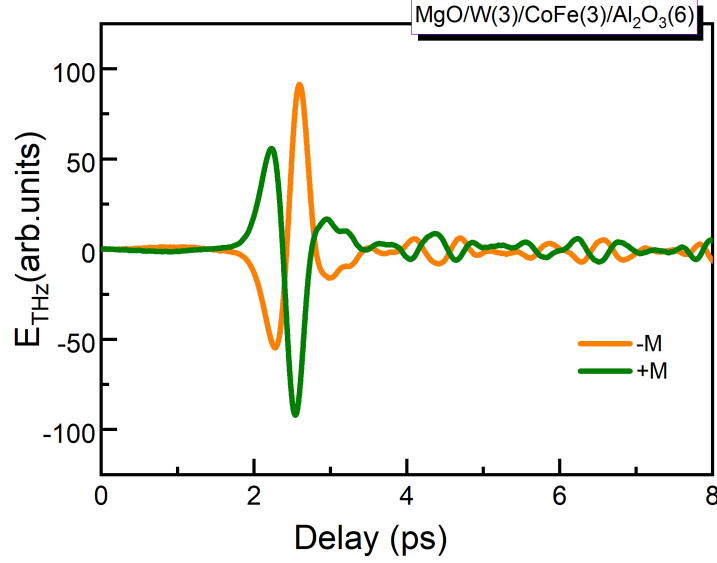


FIG. S8. THz electric field in time domain for MgO/W(3)/CoFe(3)/Al₂O₃(6) when pumping from substrate side using 0.3 mJ/cm² laser fluency. The THz signal is inverted when the magnetization direction is reversed.

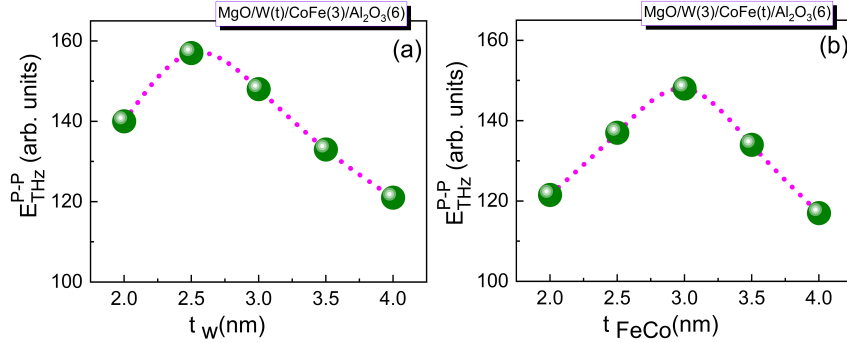


FIG. S9. (a) THz electric field peak-to-peak amplitude for MgO/W(t_W)/CoFe(3)/Al₂O₃(6) versus thickness t_W of the tungsten layer. (b) THz electric field peak-to-peak amplitude for MgO/W(3)/CoFe(t_{CoFe})/Al₂O₃(6) versus thickness t_{CoFe} of the CoFe layer.

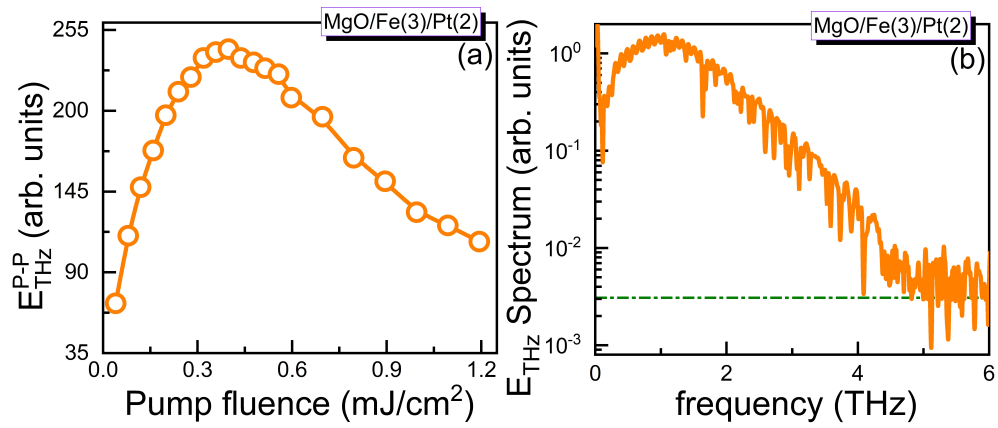


FIG. S10. (a) THz electric field peak-to-peak amplitude for MgO/Fe(3)/Pt(2) when pumping from substrate side using $0.3 \text{ mJ}/\text{cm}^2$ laser fluency. (b) Fast Fourier transform of time-domain signal for MgO/Fe(3)/Pt(2).

V. TRANSMITTANCE, REFLECTANCE AND ABSORPTION RESULTS

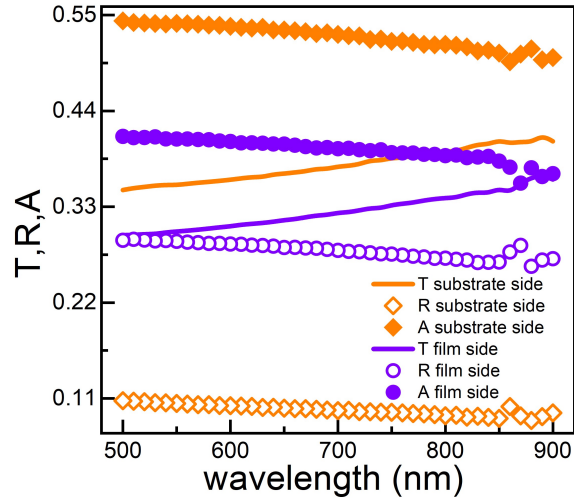


FIG. S11. Transmittance (T), reflectance (R) and absorption (A) versus wavelength for $W(3)/CoFe(2.5)/Al_2O_3(6)$ grown on single sided polished Al_2O_3 .

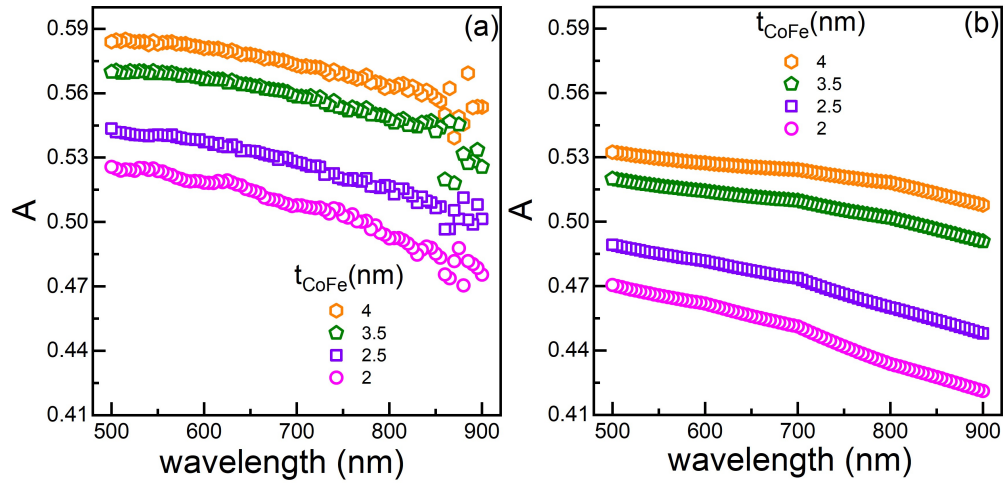


FIG. S12. Absorption spectra for sapphire/ $W(3)/CoFe(t_{CoFe})/Al_2O_3(6)$; (a) experimental and (b) calculated results.

VI. COMPARISON THZ EMISSION USING DOUBLE-SIDED AND SINGLE-SIDED POLISHED SUBSTRATES

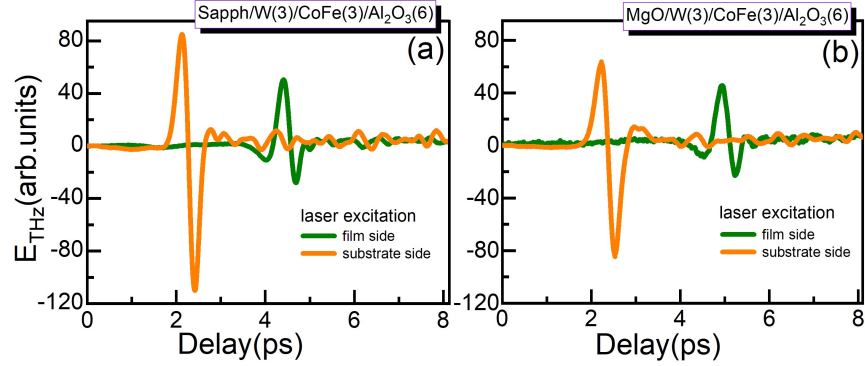


FIG. S13. THz electric field in time domain for sapph/W(3)/CoFe(3)/Al₂O₃(6) and MgO/W(3)/CoFe(3)/Al₂O₃(6) when pumping from substrate and film sides using 0.3 mJ/cm² laser fluency. The former STE was grown on a double-sided polished substrate, while the latter was grown on a single-sided polished substrate; the THz electric field amplitude is significantly larger for the film grown on the double-sided polished substrate.

VII. X-RAY REFLECTIVITY

To quantify the W (t_W^E) and CoFe (t_{CoFe}^E) thicknesses, substrate-film interface roughness ($\sigma_{substrate/W}$), W-CoFe interface roughness ($\sigma_{W/CoFe}$) and film-capping interface roughness ($\sigma_{CoFe/capping}$) in our emitters, we utilized x-ray reflectivity (XRR) measurements. The XRR spectra were recorded in the range of $2\theta=(0^\circ-6^\circ)$. The layer thickness and interface roughness were investigated by simulating the XRR spectra using the GenX software. The estimated values of layer thicknesses and both interface roughnesses for all emitters are presented in Tables ST1-ST4.

TABLE ST1. Comparison of nominal (t_W^N) and GenX extracted thickness (t_W^E) from XRR analysis for films grown on MgO(001) substrates. The nominal thickness of the CoFe layer was $t_{CoFe}^N = 30 \text{ \AA}$. The thickness and roughness are in \AA .

t_W^N	$\sigma_{substrate/W}$	t_W^E	$\sigma_{W/CoFe}$	t_{CoFe}^E	σ_{CoFe/Al_2O_3}	$t_{Al_2O_3}^E$
40	3	38	1	26	5	58
35	2	34	1	26	4	59
30	2	29	1	29	12	56
25	2	24	0	28	8	58
20	3	20	1	26	5	59

TABLE ST2. Comparison of nominal (t_W^N) and GenX extracted thickness (t_W^E) from XRR analysis for films grown on $Al_2O_3(11\bar{2}0)$ substrates. The nominal thickness of the CoFe layer was $t_{CoFe}^N = 30 \text{ \AA}$. The thickness and roughness are in \AA .

t_W^N	$\sigma_{substrate/W}$	t_W^E	$\sigma_{W/CoFe}$	t_{CoFe}^E	σ_{CoFe/Al_2O_3}	$t_{Al_2O_3}^E$
40	5	41	5	25	5	58
35	1	35	4	25	4	57
30	8	31	5	26	6	57
25	1	25	3	26	5	57
20	10	21	3	24	4	60

TABLE ST3. Comparison of nominal (t_{CoFe}^N) and GenX extracted thickness (t_{CoFe}^E) from XRR analysis for films grown on MgO(001) substrates. The nominal thickness of the W layer was $t_W^N = 30$ Å. The thickness and roughness are in Å.

t_{CoFe}^N	$\sigma_{substrate/W}$	t_W^E	$\sigma_{W/CoFe}$	t_{CoFe}^E	σ_{CoFe/Al_2O_3}	$t_{Al_2O_3}^E$
40	1	29	1	30	6	64
35	2	29	1	29	8	61
30	2	29	1	29	12	56
25	2	29	1	19	2	63
20	3	28	2	18	3	65

TABLE ST4. Comparison of nominal (t_{CoFe}^N) and GenX extracted thickness (t_{CoFe}^E) from XRR analysis for films grown on Al₂O₃(11 $\bar{2}$ 0) substrates. The nominal thickness of the W layer was $t_W^N = 30$ Å. The thickness and roughness are in Å.

t_{CoFe}^N	$\sigma_{substrate/W}$	t_W^E	$\sigma_{W/CoFe}$	t_{CoFe}^E	σ_{CoFe/Al_2O_3}	$t_{Al_2O_3}^E$
40	2	31	3	33	5	58
35	10	30	4	28	4	58
30	8	31	5	26	6	57
25	10	30	3	20	4	59
20	10	30	3	19	6	54